coatings

MDPI

Communication

Effect of Various Metal Oxide Insulating Layers on the Magnetic Properties of Fe-Si-Cr Systems

Zhenyi Huang [1], Huaqin Huang [2], Hao He [2], Zhaoyang Wu [1], Xuesong Wang [1,*] and Rui Wang [2,*]

[1] School of Metallurgical Engineering, Anhui University of Technology, Maanshan 243002, China; huangzhenyi@ahut.edu.cn (Z.H.)
[2] Key Laboratory of Green Fabrication and Surface Technology of Advanced Metal Materials, Anhui University of Technology, Ministry of Education, Maanshan 243002, China
* Correspondence: wangxs@ahut.edu.cn (X.W.); worry@ahut.edu.cn (R.W.)

Abstract: Iron-based soft magnetic composites (SMCs) are the key components of high-frequency electromagnetic systems. Selecting a suitable insulating oxide layer and ensuring the integrity and homogeneity of the heterogeneous core–shell structure of SMCs are essential for optimizing their magnetic properties. In this study, four types of SMCs—Fe-Si-Cr/ZrO_2, Fe-Si-Cr/TiO_2, Fe-Si-Cr/MgO, and Fe-Si-Cr/CaO—were prepared via ball milling, followed by hot-press sintering. The differences between the microscopic morphologies and magnetic fproperties of the Fe-Si-Cr/AO_x SMCs prepared using four different metal oxides were investigated. ZrO_2, TiO_2, MgO, and CaO were successfully coated on the surface of the Fe-Si-Cr alloy powders through ball milling, forming a heterogeneous Fe-Si-Cr/AO_x core–shell structure with the Fe-Si-Cr alloy powder as the core and the metal oxide as the shell. ZrO_2 is relatively hard and less prone to breakage and refinement during ball milling, resulting in a lower degree of agglomeration on the surface of the composites and prevention of peeling and collapse during hot-press sintering. When ZrO_2 was used as the insulation layer, the magnetic dilution effect was minimized, resulting in the highest resistivity (4.2 mΩ·cm), lowest total loss (580.8 kW/m^3 for $P_{10mt/100kHz}$), and lowest eddy current loss (470.0 kW/m^3 for $P_{ec\ 10mt/100kHz}$), while the permeability stabilized earlier at lower frequencies.

Keywords: metal oxide; insulating layers; soft magnetic composites; magnetic properties

Citation: Huang, Z.; Huang, H.; He, H.; Wu, Z.; Wang, X.; Wang, R. Effect of Various Metal Oxide Insulating Layers on the Magnetic Properties of Fe-Si-Cr Systems. *Coatings* **2023**, *13*, 804. https://doi.org/10.3390/coatings13040804

Academic Editor: Giovanni Ausanio

Received: 24 March 2023
Revised: 11 April 2023
Accepted: 12 April 2023
Published: 20 April 2023

1. Introduction

Iron-based soft magnetic composites (SMCs), which are characterized by high saturation magnetization, high permeability, and low core losses, are the key components of high-frequency electromagnetic systems [1,2]. With the development of frequency control technology, the further reduction in losses in the energy conversion of iron-based SMCs is the key to achieving the miniaturization and efficient application of high-frequency devices [3]. The preparation of iron-based SMCs involves the formation of a heterogeneous core–shell structure by coating the surface of iron-based alloy powders with an insulating layer, either physically or chemically, followed by hot-press sintering and heat treatment. Although optimizing the composition of iron-based alloy powders leads to improved magnetic conductivity of iron-based SMCs, a high-quality insulation layer is essential for ameliorating high-frequency energy losses [4]. Therefore, the selection of a suitable insulating layer is among the most important considerations in the design and development of iron-based SMCs.

In recent years, organic insulators such as polyimide [5], silicone resin [6], and epoxy resin [7] have been widely utilized in industrial production owing to their favorable adhesion and extensibility properties; however, their poor thermal stability limits their practical applicability. To overcome the shortcomings of organic insulating layers when utilized in iron-based SMCs, researchers have used metal oxides (AO_x) such as MgO [8], ZrO_2

[9], MnO_2 [10], and Al_2O_3 [11] as insulating layers given their high thermal stability and resistivity, which are strongly dependent on point defects [12–14]. For example, Wei et al. [15] deposited MgO cladding on an Fe-Si-Al alloy powder, which resulted in a permeability of 74.49 and a loss of 414.76 mW/cm^3 at 50 kHz. Dong et al. [16] coated TiO_2 onto the surface of amorphous FeSiBCCr powders via hydrolysis and condensation reactions, and the resultant composite displayed a permeability of 67 and a loss of 265 mW/cm^3 at 5 mT and 100 kHz. Yan et al. [9] employed mechanical ball milling to uniformly coat ZrO_2 particles on the surface of iron powder, which led to enhanced resistivity (225.76 μΩ/cm) and a significant reduction in the eddy current loss; however, the ball milling process increased the occurrence of defects and stresses. Choi et al. [17] prepared Al_2O_3 insulating layers of varying thicknesses on the surface of Fe-Si-Cr alloy powders using the sol-gel method, thereby fabricating a composite with an effective permeability of 33.9 and a loss of 252 mW/cm^3 at 50 mT and 100 kHz. Although previous studies [18–21] have demonstrated that metal oxides are promising candidates for use as insulating layers in the production of Fe-based SMCs, recent studies have predominantly focused on developing new metal oxide insulating layers and improving the properties of Fe-based SMCs [22,23].

The effects of specific metal oxide insulating layers on the magnetic properties of homogeneous iron-based SMCs have not yet been investigated. In this study, various metal oxides were used as insulation layers (AO_x) to coat Fe-Si-Cr alloy powder by simple mechanical ball milling, followed by the preparation of Fe-Si-Cr/AO_x SMCs via hot-press sintering and heat treatment. The results of our study provide valuable insights for the development of efficient iron-based SMCs that possess high power densities and are amenable to miniaturization.

2. Materials and Methods

2.1. Materials and Reagents

Fe-Si-Cr alloy powder (Si = 5.51 wt.%, Cr = 4.98 wt.%, average particle size of 23.78 μm with a standard deviation of 6.140), produced via gas atomization, was sourced from Changsha Tijo Metal Material Co., Ltd. (Changsha, China) CaO, MgO, TiO_2, and ZrO_2 powders (purity ≥ 99.9%, average particle size: 100–300 nm) were purchased from Sinopharm Chemical Reagent Co., Ltd. (Shanghai, China). High-purity argon (purity ≥ 99.99%, Nanjing Special Gas Factory Co., Ltd. (Nanjing, China)) was used as the protective gas during the heat treatment process.

2.2. Experimental Process

2.2.1. Material Preparation

First, the Fe-Si-Cr alloy and metal oxide (CaO, MgO, TiO_2, or ZrO_2) powders were placed in stainless-steel ball mill jars at a mass ratio of 10:1, ball-to-material ratio of 8:1, and ball-milled at a rate of 300 rpm for 1 h to prepare the Fe-Si-Cr/AO_x composite powders. The Fe-Si-Cr/AO_x composite powder was then placed in a graphite mold and sintered in an SM-100E electrically pressurized sintering machine (Hubei Precision Materials Technology Co., Ltd. Huangshi, China). The sintering temperature was increased from 25 °C to 900 °C within 10 min and maintained at this level for 10 min at a pressure of 14 MPa. After sintering, the SMCs were annealed at 650 °C for 120 min [22]. The final dimensions of the prepared Fe-Si-Cr/AO_x SMCs were 5 mm in height with outer and inner diameters of 30 and 20 mm, respectively.

2.2.2. Material Characterization

The physical phases of the Fe-Si-Cr alloy powder and Fe-Si-Cr/AO_x composite powders were analyzed on a Bruker D8 Advance X-ray diffractometer (XRD, Bruker, Berlin, Germany) within the 2θ range of 10–90° at a scan rate of 1 (°)/min. The surface and sectional morphologies and compositional distributions of the Fe-Si-Cr/AO_x composite powders and SMCs were characterized by scanning electron microscopy (SEM, Tescan Mira3

Xmu, TESCAN, Prague, Czech Republic) combined with energy-dispersive X-ray spectroscopy (EDS). The electronic structures of the oxide elements in the Fe-Si-Cr/AO_x soft magnetic composite cores were investigated by XPS (ULVAC-PHI, Tokyo, Japan) and with a PHI-5000 Versaprobe instrument. The hysteresis loops of the Fe-Si-Cr/AO_x SMCs were analyzed at 25 °C using an MPMS-3 vibrating sample magnetometer (VSM, Quantum Design, San Diego, CA, USA) with an external field range of ±20,000 Oe and a step size of 50 Oe. A four-point probe system (RTS-8, Suzhou Jingge Electronics Co., Ltd., Suzhou, China) and an AC magnetic analyzer (SY-8219, IWATSU, Tokyo, Japan) were used to characterize the resistivity and loss of the Fe-Si-Cr/AO_x SMCs. The hardness was measured using a hardness tester (HRS-150, Shanghai Optical Instrument Factory, Shanghai, China).

3. Results and Discussion

3.1. Microstructure of Fe-Si-Cr/AO_x Composite Powders and SMCs

Figure 1 shows the XRD patterns of raw Fe-Si-Cr and Fe-Si-Cr/AO_x composite powders coated with various metal oxides. The diffraction peaks at 2θ = 44.73°, 65.12°, and 82.48° in the profile of the raw Fe-Si-Cr alloy powder correspond to the (110), (200), and (211) crystal planes of the α-Fe (Si, Cr) phase in the body-centered cubic structure, respectively, according to the JPCDS standard card 06-0696 [24]. In contrast, new diffraction peaks were observed in the XRD patterns of the Fe-Si-Cr/AO_x composite powders in addition to the three diffraction peaks of the-Fe (Si, Cr) phase. For example, the new diffraction peaks at 2θ = 28.18 and 31.44° for the ZrO_2-coated composite powder correspond to the (−111) and (111) crystal planes of monoclinic ZrO_2 (JCPDS Standard Card 27-0997) [25]. The peak at 2θ = 25.41° corresponds to the (101) crystal plane diffraction of anatase TiO_2, while that at 2θ = 42.94°, 62.34° corresponds to the (200) and (220) crystal plane diffraction of the cubic magnesite structure MgO at 2θ = 32.18°. The diffraction peaks at 37.39° and 53.82° correspond to the (111), (200), and (220) crystal planes of the face-centered cubic structure of CaO, respectively. The peaks attributed to the metal oxides are unambiguous, and no other spurious peaks are observed. Furthermore, the position (44.71°, 65.10°, 82.44°) and half-height width (0.29, 0.49, 0.58) of the characteristic peaks of the α-Fe (Si, Cr) phase were minimally altered after coating with the metal oxides, while the crystallite sizes were almost same (31.03–31.77 nm), indicating that the Fe-Si-Cr/AO_x composite powder prepared by ball milling did not affect the crystal structure of the Fe-Si-Cr alloy powder substrate.

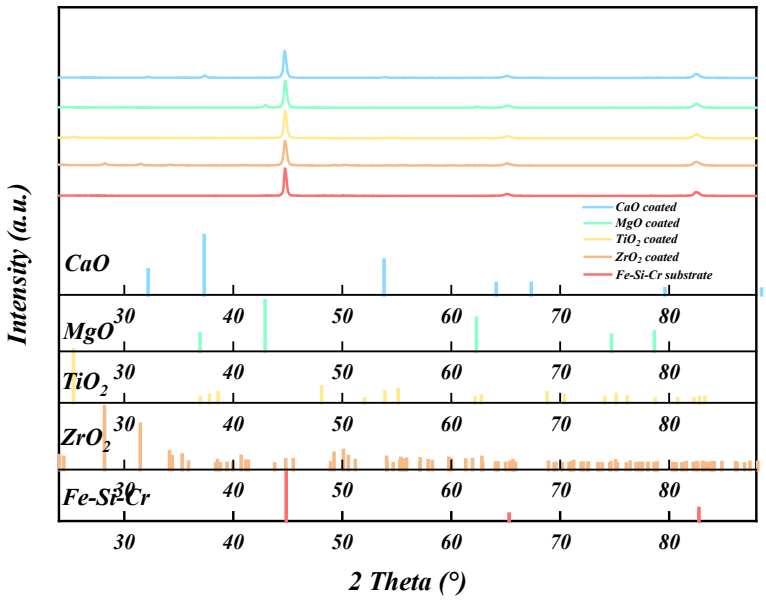

Figure 1. XRD spectra of raw Fe-Si-Cr alloy powder and Fe-Si-Cr/AO_x composite powders comprising varying metal oxide insulating layers.

To further investigate the effect of each metal oxide layer on the morphological characteristics of the Fe-Si-Cr/AO_x composite powders, their surface morphologies and elemental distributions were analyzed by SEM and EDS, and the results are shown in Figure 2. The surfaces of the raw Fe-Si-Cr alloy powders (Figure 2a) were generally smooth, showing some defects such as pits produced during gas atomization. In comparison, the dimensions of the Fe-Si-Cr/AO_x composite powders changed negligibly but were slightly deformed after depositing the metal oxide insulating layers by ball milling, owing to the plastic deformation of the Fe-Si-Cr substrate resulting from collisions during the ball milling process. The surface of the Fe-Si-Cr/AO_x composite powder was rough and covered with numerous agglomerated small particles. The pit defects visible on the surface of the pristine powder substrate were filled with oxide particles. The EDS analysis indicated that Zr, Ti, Mg, Ca, and O were distributed over the entire surface of the Fe-Si-Cr/AO_x composite powders. This suggests that each of the corresponding metal oxides, CaO, MgO, TiO_2, and ZrO_2, formed an insulation layer on the surface of the Fe-Si-Cr alloy powders, constituting a heterogeneous core–shell structure comprising the Fe-Si-Cr alloy powder as the core and AO_x as the shell. This powdered raw material was used for the preparation of Fe-Si-Cr/AO_x SMCs. The combined SEM and EDS results further indicated that the uniformity and integrity of the insulation layer were the most and least favorable when ZrO_2 and CaO were utilized, respectively. This is because the metal oxide powder gradually broke down and was refined during ball milling. Therefore, the lower the hardness, the easier it is to form an ultrafine powder, resulting in increased surface energy of the powder. Consequently, a more unstable energy state is attained, leading to an increase in the agglomeration coefficient. The hardness of the four metal oxides decreased in the following order: ZrO_2 (7.5 Mohs) > TiO_2 (6.0 Mohs) > MgO (5.5 Mohs) > CaO (1.6 Mohs) [26–29]. Lower hardness can result in agglomeration, which occurs more easily during the pressing process, resulting in an uneven coating. Consequently, the degree of agglomeration on the surface of the Fe-Si-Cr/CaO substrate after ball milling increased and the quality of the insulation layer deteriorated.

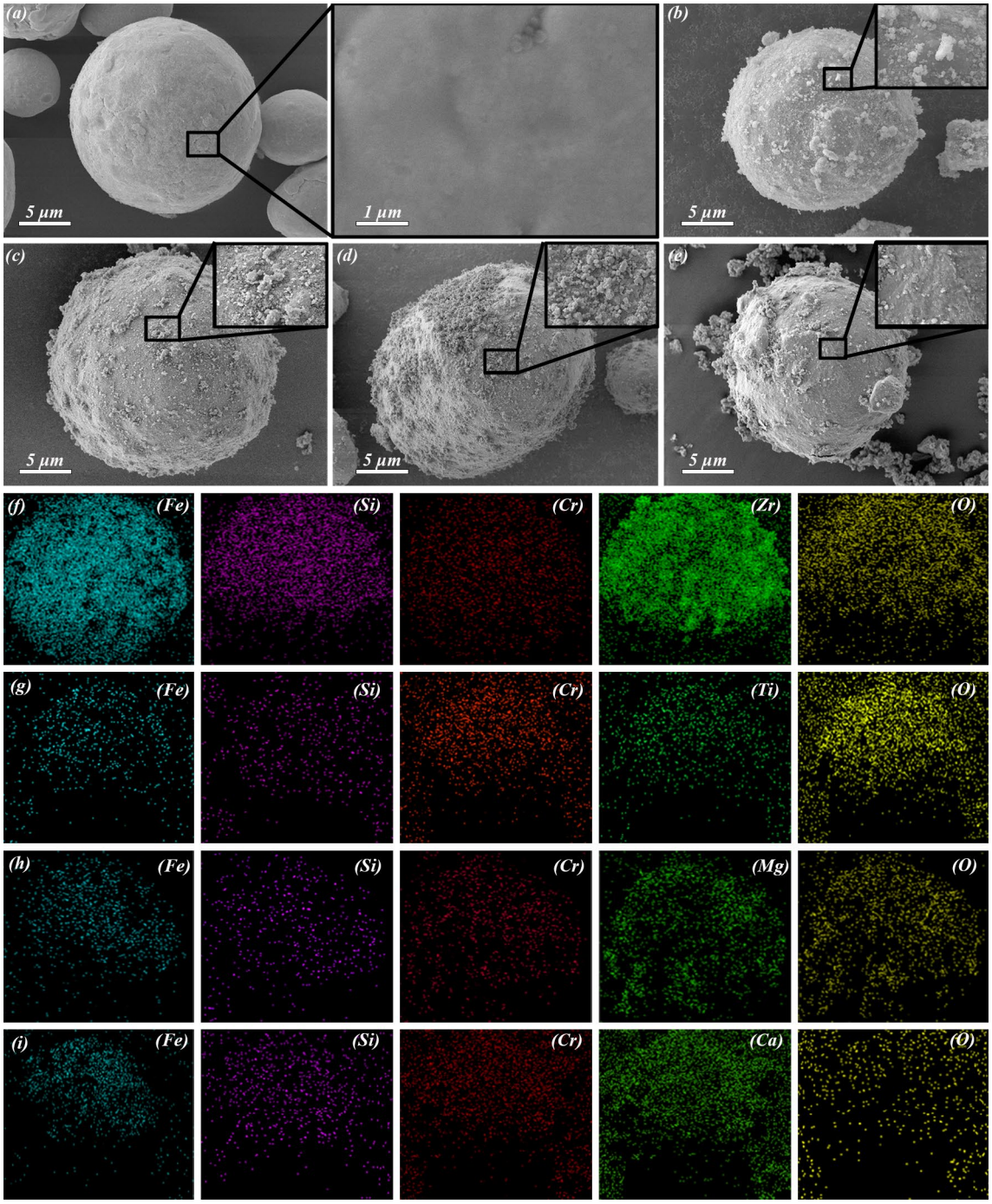

Figure 2. SEM images and EDS results showing the surface morphology and elemental distribution of (**a**) raw Fe-Si-Cr alloy powder and (**b–i**) Fe-Si-Cr/AO_x composite powders coated with varying metal oxide layers. (**b**,**f**) Fe-Si-Cr/ZrO_2, (**c**,**g**) Fe-Si-Cr/TiO_2, (**d**,**h**) Fe-Si-Cr/MgO, and (**e**,**i**) Fe-Si-Cr/CaO.

Backscattered SEM images of the Fe-Si-Cr/AO_x SMCs with polished sections obtained after sintering and annealing are shown in Figure 3. Backscattered electrons are sensitive to the atomic number of the material; the higher the atomic number, the brighter the corresponding backscattered electron image. The elemental distribution signals showed that Fe was mainly concentrated in the internal Fe-Si-Cr substrate region, whereas O as well as Zr, Ti, Mg, and Ca derived from ZrO_2, TiO_2, MgO, and CaO were predominantly distributed at the interface. This indicated that the heterogeneous Fe-Si-Cr/AO_x core–shell structure was successfully assembled to form SMCs. A comparison of the Fe-Si-Cr/AO_x

SMCs comprising four different metal oxide coatings revealed that the insulating layers of Fe-Si-Cr/ZrO_2 (Figure 3a) and Fe-Si-Cr/TiO_2 (Figure 3b) were complete and relatively uniform in thickness. However, the insulating layers of Fe-Si-Cr/MgO (Figure 3c) and Fe-Si-Cr/CaO (Figure 3d) were non-uniformly distributed, with some porosity and agglomeration due to the frictional force between the Fe-Si-Cr/AO_x core–shell heterostructure composite powders [30]. During sintering, the composite powders collided and were compressed, thus reducing the gaps between the powder particles. The hardness values of MgO and CaO are lower than those of ZrO_2 and TiO_2. Due to the low hardness, CaO and MgO agglomerate during the pressing process, and the insulating layer that originally covered the powder is detached, resulting in the formation of pores between the spherical powder powders.

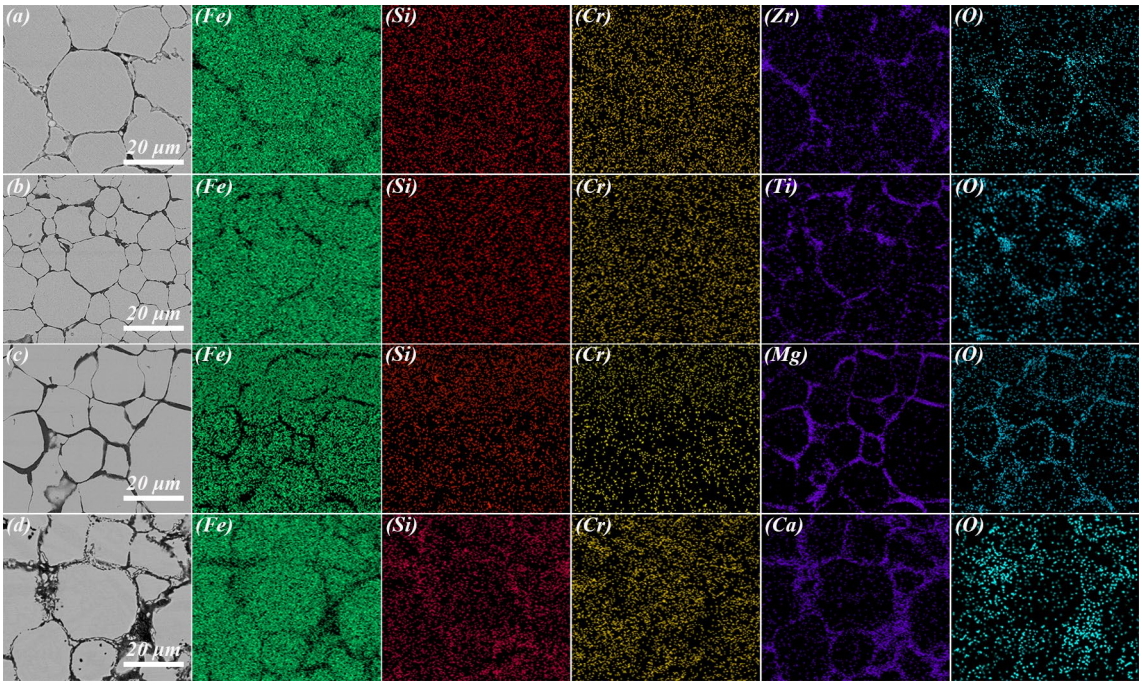

Figure 3. BSE images and EDS energy spectra of Fe-Si-Cr/AO_x soft magnetic composite cores: (**a**) Fe-Si-Cr/ZrO_2, (**b**) Fe-Si-Cr/TiO_2, (**c**) Fe-Si-Cr/MgO, and (**d**) Fe-Si-Cr/CaO.

Figure 4 shows the XPS data for the Fe-Si-Cr/AO_x SMCs' polished section, which comprised four different types of metal oxides as insulating layers. The corrected positions of Zr3d (Figure 4a), Ti2p (Figure 4b), Mg1s (Figure 4c), and Ca2p (Figure 4d) were obtained by curve fitting and setting the electron binding energy of the C1s peak to 284.8 eV. The two fitted peaks of Zr [31,32] at 181.46 and 183.81 eV correspond to the two split peaks of $Zr3d_{5/2}$ and $Zr3d_{3/2}$, respectively. The two fitted peaks of Ti [33,34] at 458.26 and 463.92 eV correspond to the two split peaks of $Ti2p_{3/2}$ and $Ti2p_{1/2}$ respectively; the fitted peaks of Mg [35] for the Mg1s orbital with a binding energy of 1304.13 eV correspond to the Mg-O structure, while the two spin split peaks of $Ca2p_{3/2}$ and $Ca2p_{1/2}$ at 346.72 and 350.29 eV [36] indicate the presence of Ca-O. The XPS results verified the SEM and EDS results for the Fe-Si-Cr/AO_x SMCs. This indicates that the corresponding Zr, Ti, Mg, and Ca elements in the four metal oxides, ZrO_2, TiO_2, MgO, and CaO, were mainly distributed at the interface and that the core–shell heterostructure of the SMCs did not collapse during the sintering process.

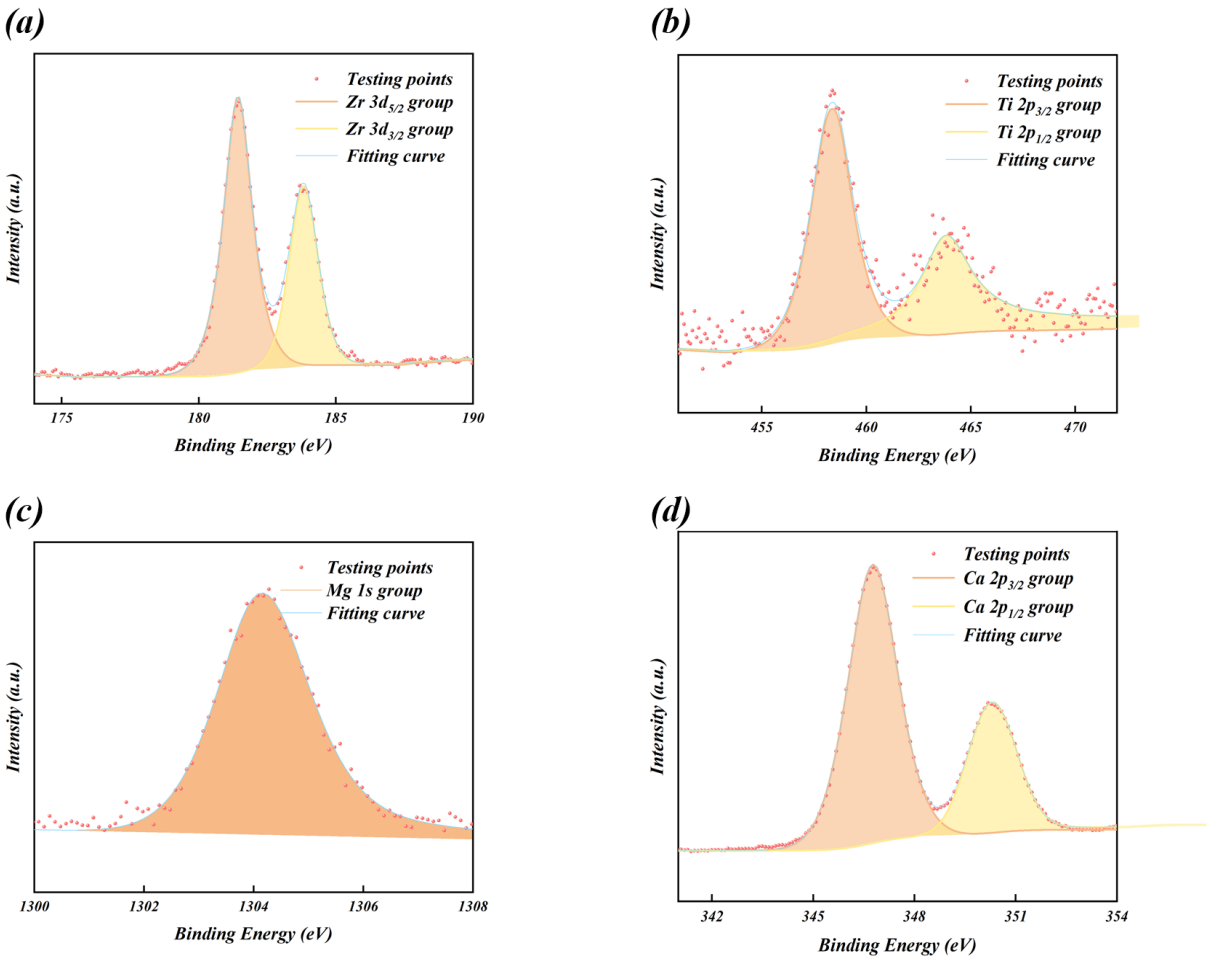

Figure 4. XPS profiles of oxide metal elements in Fe-Si-Cr/AO_x soft magnetic cores: (**a**) Zr, (**b**) Ti, (**c**) Mg, and (**d**) Ca.

3.2. Effect of Distinct Metal Oxide Insulating Layers on the Magnetic Properties of the SMCs

Figure 5a,b shows the saturation magnetization hysteresis loops and magnified areas of the curves for the Fe-Si-Cr SMCs, respectively. Although the metal oxide insulating layers differ, all the corresponding soft magnetic composite cores exhibit similar characteristics, that is, high saturation magnetization strength (M_s) and low coercivity (H_c) and remanence (M_r). The magnetic susceptibilities of all the Fe-Si-Cr/AO_x SMCs became saturated when the applied magnetic field strength reached 15,000 Oe. However, the M_s values of the SMCs were generally lower than those of the Fe-Si-Cr soft magnetic cores (200.1 emu/g). This is because M_s values are derived from the static magnetic properties of the material energy. Furthermore, because the metal oxide insulation layer is a nonmagnetic phase, its introduction leads to a reduction in the number of total magnetic moments per unit volume of the core [37]. Owing to the superior homogeneity and integrity of the metal oxide insulating layer and fewer internal pores in the Fe-Si-Cr/ZrO_2 SMCs (184.2 emu/g) and Fe-Si-Cr/TiO_2 SMCs (186.9 emu/g) composite cores, the saturation magnetization strengths of these samples were higher than those of the Fe-Si-Cr/MgO SMCs (180.5 emu/g) and Fe-Si-Cr/CaO SMCs (177.6 emu/g). The coercivity of SMCs is an inherent property affected by the number and strength of magnetic dipole moments and the interaction between adjacent magnetic domains. There was no significant difference between the coercivities of the Fe-Si-Cr/AO_x SMCs, indicating that the nonmagnetic metal oxide insulating layers and the heterogeneous Fe-Si-Cr/AO_x core–shell structures did not significantly affect the magnetic domains.

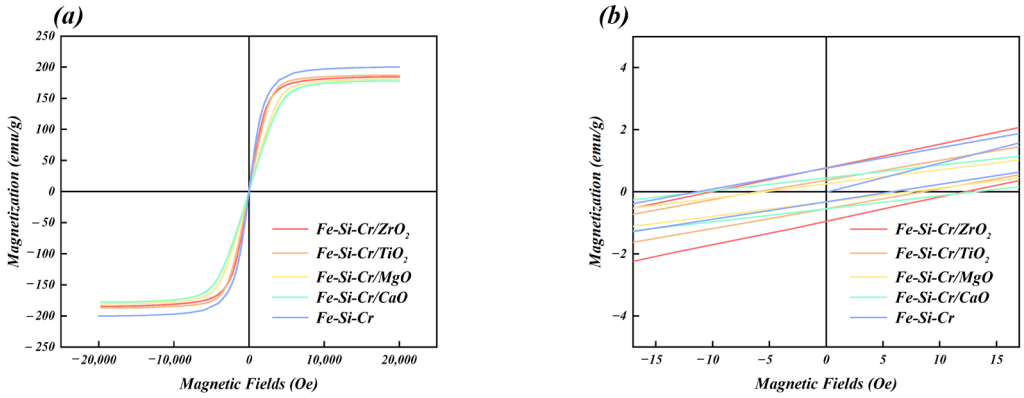

Figure 5. (**a**) Saturation magnetization hysteresis loops and (**b**) local magnification of curves for Fe-Si-Cr SMCs and Fe-Si-Cr/AO_x soft magnetic composite cores at room temperature.

Quantitative analysis of the uniformity of the insulating layer of SMCs is difficult. However, a more uniform insulating layer can suppress interparticle eddy currents more effectively, improve the electrical insulation between alloy powders, and reduce the magnetic dilution phenomenon caused by the agglomeration of nonmagnetic substances [38]. Therefore, in this study, the effects of four metal oxide insulating layers on the insulating properties of Fe-Si-Cr/AO_x SMCs were investigated by introducing resistivity. The results are shown in Figure 6a. The resistivity of the Fe-Si-Cr/AO_x SMCs coated with four metal oxide insulating layers was higher than that of the Fe-Si-Cr SMCs. Furthermore, the Fe-Si-Cr/ZrO_2 SMCs and Fe-Si-Cr/TiO_2 SMCs with uniform and compact insulating layers exhibited higher resistivities. This may be due to the high temperature and pressure during sintering, which promoted the growth of ZrO_2 grains [39] and improved the homogeneity of the insulating layer. The high-temperature and high-pressure sintering environment also promotes the crystallization of TiO_2, providing additional carrier channels and reducing the carrier concentration; consequently, the insulating characteristics of the corresponding SMCs are significantly improved [40]. Although the inhomogeneity of the insulating layer deteriorates the insulation characteristics of SMCs, the presence of pores therein can suppress this phenomenon. Therefore, the resistivities of the Fe-SMCs-Cr/MgO and Fe-Si-Cr/CaO SMCs did not decrease significantly as compared to those of the Fe-Si-Cr/ZrO_2 SMCs and Fe-Si-Cr/TiO_2 SMCs. Figure 6b shows the variation in the permeability of Fe-Si-Cr and Fe-Si-Cr/AO_x SMCs with frequency. Although the permeabilities of both the Fe-Si-Cr and Fe-Si-Cr/AO_x SMCs decreased with increasing test frequency, the permeability of the latter was more stable than that of the former. The Fe-Si-Cr/AO_x SMCs exhibited better frequency stability than the Fe-Si-Cr sample. The Fe-Si-Cr/TiO_2 SMCs with a more uniform and compact insulation layer displayed higher permeability than Fe-Si-Cr/MgO and Fe-Si-Cr/CaO SMCs, which had less uniform insulating layers. This is because a more continuous and dense insulation layer ensures the integrity of the internal magnetic domain structure of SMCs. Conversely, the accumulation of pores and oxides in Fe-Si-Cr/MgO and Fe-Si-Cr/CaO SMCs enhances the magnetic dilution effect, prevents contact between the alloy powder particles, and increases the magnetic resistance [41]. Although the permeability of the Fe-Si-Cr/ZrO_2 core was lower than that of the Fe-Si-Cr/MgO core up to 30 kHz, the decrease in permeability became less pronounced at higher operating frequencies. At >30 kHz, the permeability of Fe-Si-Cr/ZrO_2 exceeded that of Fe-Si-Cr/MgO because the intact insulation layer enhanced the depth of the skin effect, which allowed the SMCs to stabilize at lower operating frequencies.

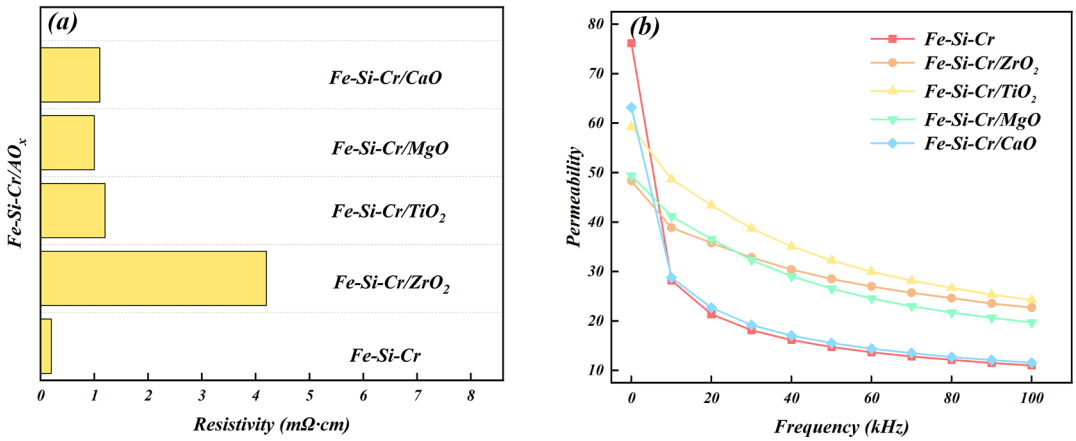

Figure 6. (**a**) Resistivity and (**b**) permeability of the Fe-Si-Cr soft magnetic core and Fe-Si-Cr/AO_x soft magnetic composite cores.

Figure 7a shows the total loss (P_{cv}) distributions of the Fe-Si-Cr and Fe-Si-Cr/AO_x SMCs under an external field of 10 mT. Evidently, the P_{cv} values of both the Fe-Si-Cr and Fe-Si-Cr/AO_x SMCs increased with frequency. For Fe-Si-Cr/ZrO_2, having more uniform insulating layers with superior integrity, the P_{cv} value (580.7 kW/m^3, at 10 mT external field, 100 kHz test frequency) decreased by ~62.6% compared to that of Fe-Si-Cr (1552.8 kW/m^3). In contrast, P_{cv} of the Fe-Si-Cr/CaO SMCs (1446.8 kW/m^3), which had inferior-quality insulating layers and increased porosity, decreased by 6.8% compared to that of the Fe-Si-Cr SMCs.

According to the classical Bertotti loss separation theory [41], P_{cv} can be divided into two parts: the hysteresis loss (P_{hyst}) and eddy current loss (P_e).

$$P_{cv} = K_h f + K_e f^m \quad (1)$$

K_h is the hysteresis loss coefficient, K_e is the eddy current loss coefficient, and f is the frequency. At a fixed magnetic field strength of m = 2, the eddy current loss was proportional to the square of the operating frequency, whereas the hysteresis loss was proportional to the operating frequency. First, the P_{cv}/f versus f curve was fitted using a linear fitting method. The fitted curve was extrapolated to the zero-frequency point to obtain the intercept of the hysteresis loss under quasi-static conditions, which was multiplied by the frequency to obtain the hysteresis loss at that frequency, as shown in Figure 7b. The eddy-current loss was obtained by subtracting the total loss from the fitted hysteresis loss, as shown in Figure 7c. The P_{hyst} values of all Fe-Si-Cr/AO_x SMCs increased almost linearly with frequency, while the discontinuous metal oxide insulating layer caused the pores inside the SMCs to restrict domain wall motion. Therefore, the Fe-Si-Cr/MgO and Fe-Si-Cr/CaO SMCs displayed higher hysteresis losses than the Fe-Si-Cr/ZrO_2 and Fe-Si-Cr/TiO_2 SMCs. Furthermore, the heterogeneous Fe-Si-Cr/AO_x core–shell structure affected the loss of the SMCs, mainly by reducing the eddy current loss by enhancing the resistivity and limiting the effective operating diameter of the eddy currents. Hence, TiO_2 and ZrO_2 insulating layers were more effective than MgO and CaO in reducing the eddy current loss in SMCs.

A comprehensive comparison of the magnetic properties indicated that for equal amounts of each metal oxide, the sintered ZrO_2 insulating layer was denser and more homogeneous than the layers derived from common metal oxides such as MgO, CaO, and TiO_2. This minimized the magnetic dilution effect and led to the highest resistivity (4.2 mΩ·cm), lowest total loss ($P_{10mt/100kHz}$ of 580.8 kW/m^3), and lowest eddy current loss (470.0 kW/m^3 for $P_{ec\ 10mt/100kHz}$) in the corresponding SMCs, while the permeability stabilized earlier at lower frequencies.

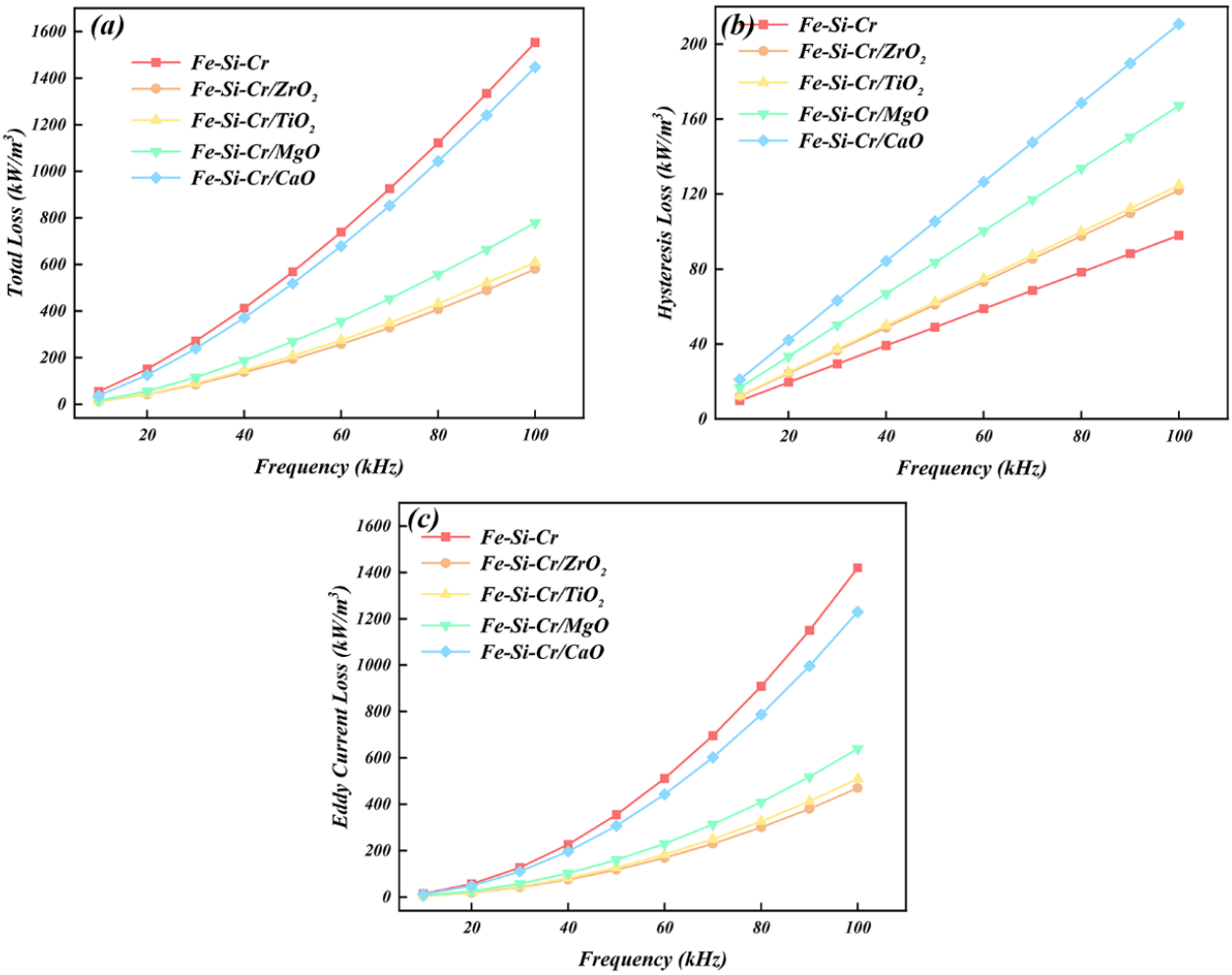

Figure 7. (**a**) Total loss, (**b**) hysteresis loss, and (**c**) eddy current loss of Fe-Si-Cr soft magnetic core and Fe-Si-Cr/AO_x soft magnetic composite cores at 10 mT.

4. Conclusions

By studying the differences between the microscopic morphologies and magnetic properties of Fe-Si-Cr/AO_x SMCs prepared using various metal oxides as insulating layers, the following conclusions were drawn:

1. Four metal oxides, ZrO_2, TiO_2, MgO, and CaO, were successfully coated on the surface of the Fe-Si-Cr alloy powder via ball milling. Thus, a heterogeneous Fe-Si-Cr/AO_x core–shell structure was formed, wherein the Fe-Si-Cr alloy powder and the metal oxides comprised the core and shell, respectively. These powdered raw materials were used for the subsequent preparation of Fe-Si-Cr/AO_x SMCs.
2. Compared to common metal oxide powders such as MgO, CaO, and TiO_2, ZrO_2 powder is harder and less prone to breakage and refinement during ball milling. This resulted in a lower degree of agglomeration on the surface of the Fe-Si-Cr alloy powder, forming an insulating layer with superior uniformity and integrity. The insulating layer resists peeling and collapse during subsequent hot pressing and heat treatment processes, ultimately providing a high-quality insulating layer for SMCs.
3. For equal amounts of each metal oxide, the sintered insulating layer comprising ZrO_2 possessed the highest density and uniformity, which minimized the magnetic dilution effect, leading to the highest resistivity (4.2 mΩ·cm) and lowest total (580.8 kW/m^3 for $P_{10mt/100kHz}$) and eddy current (470.0 kW/m^3 for $P_{ec\ 10mt/100kHz}$) losses in the corresponding SMCs. The magnetic permeability also stabilized earlier at lower frequencies (>40 kHz).

Author Contributions: Z.H., Writing—original draft, formal analysis; H.H. (Huaqing Huang), Investigation; H.H. (Hao He), Picture rendering and Review; Z.W., Performance Test; X.W., investigation and Methodology; R.W., Review, and Editing. All authors have read and agreed to the published version of the manuscript.

Funding: This work was supported by the Chinese National Science Foundation (52274311), Scientific Research Planning Project of Anhui Province (2022AH040054, 2022AH010024), and the Opening Foundation of the State Key Laboratory of Metal Material for Marine Equipment and Application (SKLMEA-K202202).

Institutional Review Board Statement: Not applicable.

Informed Consent Statement: Not applicable.

Data Availability Statement: The data presented in this study are available on request from the corresponding author.

Acknowledgments: The authors thank Chao Wang and Lei He from the Shiyanjia Lab (www.shiyanjia.com) for the XRD and XPS analyses.

Conflicts of Interest: The authors declare no conflict of interest.

References

1. Luo, Z.; Feng, B.; Chen, D.; Yang, Z.; Jiang, S.; Wang, J.; Wu, Z.; Li, G.; Li, Y.; Fan, X. Preparation and magnetic performance optimization of FeSiAl/Al_2O_3–MnO–Al_2O_3 soft magnetic composites with particle size adjustment. *J. Mater. Sci. Mater. Electron.* **2021**, *33*, 850–860.
2. Talaat, A.; Suraj, M.; Byerly, K.; Wang, A.; Wang, Y.; Lee, J.; Ohodnicki, P. Review on soft magnetic metal and inorganic oxide nanocomposites for power applications. *J. Alloys Compd.* **2021**, *870*, 159500.
3. Meng, B.; Hou, J.; Ning, F.; Yang, B.; Zhou, B.; Yu, R. Low-loss and high-induction Fe-based soft magnetic composites coated with magnetic insulating layers. *J. Magn. Magn. Mater.* **2019**, *492*, 165651.
4. Wang, J.; Song, S.; Sun, H.; Hang, G.; Xue, Z.; Wang, C.; Chen, W.; Chen, D. Insulation layer design for soft magnetic composites by synthetically comparing their magnetic properties and coating process parameters. *J. Magn. Magn. Mater.* **2021**, *519*, 165651.
5. Yuan, H.-J.; Lu, C.-X.; Zhang, S.-C.; Wu, G.-P. Preparation and characterization of a polyimide coating on the surface of carbon fibers. *New Carbon Mater.* **2015**, *30*, 115–121.
6. Wu, S.; Sun, A.; Zhai, F.; Wang, J.; Zhang, Q.; Xu, W.; Logan, P.; Volinsky, A.A. Annealing effects on magnetic properties of silicone-coated iron-based soft magnetic composites. *J. Magn. Magn. Mater.* **2012**, *324*, 818–822.
7. Jin, X.; Li, T.; Jia, Z.; Shi, H.; Xue, D. Over 100 MHz cut-off frequency mechanism of Fe-Si soft magnetic composites. *J. Magn. Magn. Mater.* **2022**, *556*, 169366.
8. Dong, B.; Qin, W.; Su, Y.; Wang, X. Magnetic properties of FeSiCr@MgO soft magnetic composites prepared by magnesium acetate pyrolysis for high-frequency applications. *J. Magn. Magn. Mater.* **2021**, *539*, 168350.
9. Geng, K.; Xie, Y.; Xu, L.; Yan, B. Structure and magnetic properties of ZrO_2-coated Fe powders and Fe/ZrO_2 soft magnetic composites. *Adv. Powder Technol.* **2017**, *28*, 2015–2022.
10. Zhang, Y.; Fan, X.; Hu, W.; Luo, Z.; Yang, Z.; Li, G.; Li, Y. Microstructure and magnetic properties of MnO_2 coated iron soft magnetic composites prepared by ball milling. *J. Magn. Magn. Mater.* **2020**, *514*, 167295.
11. Yaghtin, M.; Taghvaei, A.H.; Hashemi, B.; Janghorban, K. Effect of heat treatment on magnetic properties of iron-based soft magnetic composites with Al_2O_3 insulation coating produced by sol-gel method. *J. Alloys Compd.* **2013**, *581*, 293–297.
12. Shi, X.; Chen, X.; Wan, K.; Zhang, B.; Duan, P.; Zhang, H.; Zeng, X.; Liu, W.; Su, H.; Zou, Z.; et al. Enhanced magnetic and mechanical properties of gas atomized Fe-Si-Al soft magnetic composites through adhesive insulation. *J. Magn. Magn. Mater.* **2021**, *534*, 168040.
13. Averback, R.S.; Ehrhart, P.; Popov, A.I.; Sambeek, A.V. Defects in ion implanted and electron irradiated MgO and Al_2O_3. *Radiat. Eff. Defects Solids* **1995**, *136*, 169–173.
14. Tardío, M.; Ramírez, R.; González, R.; Chen, Y.; Kokta, M.R. Electrical conductivity in magnesium-doped Al_2O_3 crystals at moderate temperatures. *Radiat. Eff. Defects Solids* **2001**, *155*, 409–413.
15. Kotomin, E.A.; Kuzovkov, V.N.; Popov, A.I.; Vila, R. Kinetics of F center annealing and colloid formation in Al_2O_3. *Nucl. Instrum. Methods Phys. Res. Sect. B Beam Interact. Mater. At.* **2016**, *374*, 107–110.
16. Zhou, B.; Dong, Y.; Liu, L.; Chang, L.; Bi, F.; Wang, X. Enhanced soft magnetic properties of the Fe-based amorphous powder cores with novel TiO2 insulation coating layer. *J. Magn. Magn. Mater.* **2019**, *474*, 1–8.
17. Choi, S.; Lee, S.; Bon, C.Y.; Lee, K.; Choi, S.J.; Yoo, S.I. Novel Fabrication Method for a High-Performance Soft-Magnetic Composite Composed of Alumina-Coated Fe-Based Metal Powder. *J. Electron. Mater.* **2020**, *50*, 664–674.
18. Vega, L.E.R.; Leiva, D.R.; Neto, R.L.; Silva, W.B.; Silva, R.A.; Ishikawa, T.T.; Kiminami, C.S.; Botta, W.J. Improved ball milling method for the synthesis of nanocrystalline TiFe compound ready to absorb hydrogen. *Int. J. Hydrog. Energy* **2020**, *45*, 2084–2093.

19. Yuan, W.; Sun, K.; Tian, J.; Li, Y.; Wang, Z.; Liu, B.; Fan, R. Improved magnetic properties of iron-based soft magnetic composites with a double phosphate-SiO2 shells structure. *J. Mater. Sci. Mater. Electron.* **2021**, *32*, 21472–21482.
20. Luo, X.; Zhang, K.; Zhou, Y.; Wu, H.; Xie, H. In situ construction of $Fe_3Al@Al_2O_3$ core-shell particles with excellent electromagnetic absorption. *J. Colloid Interface Sci.* **2022**, *611*, 306–316.
21. Gupta, G.; Mondal, K.; Balasubramaniam, R. In situ nanocrystalline Fe–Si coating by mechanical alloying. *J. Alloys Compd.* **2009**, *482*, 118–122.
22. Wang, R.; He, Y.; Kong, H.; Wang, J.; Wu, Z.; Wang, H. Influence of sintering temperature on heterogeneous-interface structural evolution and magnetic properties of Fe-Si soft magnetic powder cores. *Ceram. Int.* **2022**, *48*, 29854–29861.
23. Qiu, Y.; Wang, R.; He, Y.; Kong, H.; Li, S.; Wu, Z. Effects of axial pressure on the evolution of core-shell heterogeneous structures and magnetic properties of Fe-Si soft magnetic powder cores during hot-press sintering. *RSC Adv.* **2022**, *12*, 19875–19884.
24. Hsiang, H.I.; Fan, L.F.; Hung, J.J. Phosphoric acid addition effect on the microstructure and magnetic properties of iron-based soft magnetic composites. *J. Magn. Magn. Mater.* **2018**, *447*, 1–8.
25. Moon, B.K.; Kwon, I.M.; Jeong, J.H.; Kim, C.S.; Yi, S.S.; Kim, P.S.; Choi, H.; Kim, J.H. Synthesis and luminescence characteristics of Eu3+-doped ZrO_2 nanoparticles. *J. Lumin.* **2007**, *122*, 855–857.
26. Le Anh, D.U.C.; Hieu, P.M.; Quang, N.M. A New Chemical Mechanical Slurry for Polishing Yttrium Aluminium Garnet Material with Magnesium Oxide, Sodium Metasilicate Pentahydrate and Zirconium Dioxide Abrasive Particles. *J. Mach. Eng.* **2023**, *23*, 5–17.
27. Li, N.-N.; Li, G.-L.; Wang, H.-D.; Kang, J.-J.; Dong, T.-S. Influence of TiO_2 content on the mechanical and tribological properties of Cr_2O_3-based coating. *Mater. Des.* **2015**, *88*, 906–914.
28. Yin, D.; Niu, X.; Zhang, K.; Wang, J.; Cui, Y. Preparation of MgO doped colloidal SiO_2 abrasive and their chemical mechanical polishing performance on c-, r-and a-plane sapphire substrate. *Ceram. Int.* **2018**, *44*, 14631–14637.
29. Klabunde, K.J.; Stark, J.; Koper, O.; Mohs, C.; Park, D.G.; Decker, S.; Jiang, Y.; Lagadic, I.; Zhang, D. Nanocrystals as stoichiometric reagents with unique surface chemistry. *J. Phys. Chem.* **1996**, *100*, 12142–12153.
30. Zheng, K.L.; Yan, P.F.; Wei, X.S.; Yan, B. Study of the nano-network structure in the friction transfer film of the hybrid reinforced aluminum-based composite. *Wear* **2022**, *494–495*, 204268.
31. Zhang, S.; Sun, J.; Xu, Y.; Qian, S.; Wang, B.; Liu, F.; Liu, X. Biological Behavior of Osteoblast-like Cells on Titania and Zirconia Films Deposited by Cathodic Arc Deposition. *Biointerphases*, **2012**, *7*, 60
32. Anderson, J.A.; Fierro, J.L.G. Bulk and Surface Properties of Copper-Containing Oxides of the General Formula $LaZr_{1-x}CuxO3$. *J. Solid State Chem.* **1994**, *108*, 305–313.
33. Bender, H.; Chen, W.; Portillo, J.; Hove, L.V.D.; Vandervorst, W. AES and XPS analysis of the interaction of Ti with Si and SiO_2 during RTA. *Appl. Surf. Sci.* **1989**, *38*, 37–47.
34. Wang, R.; Ren, J.; Wu, J.; Wu, L. Characteristics and mechanism of toluene removal by double dielectric barrier discharge combined with an Fe_2O_3/TiO_2/gamma-Al_2O_3 catalyst. *RSC Adv.* **2020**, *10*, 41511–41522.
35. Wu, C.; Wang, B.; Zheng, J.; Li, H. Study on Mineral structure transformation of coal ash at high ash melting Temperature using XPS. *Spectrosc. Spectr. Anal.* **2018**, *38*, 2296–2301.
36. Demri, B.; Muster, D. XPS study of some calcium compounds. *J. Mater. Process. Technol.* **1995**, *55*, 311–314.
37. Gemeay, A.H.; Keshta, B.E.; El-Sharkawy, R.G.; Zaki, A.B. Chemical insight into the adsorption of reactive wool dyes onto amine-functionalized magnetite/silica core-shell from industrial wastewaters. *Environ. Sci. Pollut. Res. Int.* **2020**, *27*, 32341–32358.
38. Luo, Z.; Feng, B.; Yang, Z.; Chen, D.; Jiang, S.; Wang, J.; Wu, Z.; Liu, X.; Li, G.; Li, Y. Highly enhancing electromagnetic properties in Fe-Si/MnO-SiO_2 soft magnetic composites by improving coating uniformity. *Adv. Powder Technol.* **2021**, *32*, 4846–4856.
39. Xue, Y.; Pu, G.; Yu, M.; Chen, S.; Gan, L.; Lin, L.; Yang, C.; Wang, Z.; Wang, H.; Huang, Z.; et al. Effects of air annealing treatments on the microstructure, components, and mechanical properties of magnetron sputtered Al_2O_3–Cr_2O_3–ZrO_2 composite coatings. *Ceram. Int.* **2022**, *49*, 7589–7599.
40. Jin, C.Z.; Yang, Y.; Yang, X.A.; Wang, S.B.; Zhang, W.B. Visible photocatalysis of Cr(VI) at g/L level in Si/N-TiO_2 nanocrystals synthesized by one-step co-hydrolysis method. *Chem. Eng. J.* **2020**, *398*, 125641.
41. Kocsis, B.; Varga, L.K.; Zsoldos, I. Preparation of soft magnetic composite from Fe-6.9wt%Si by different heat treatment strategies. *IOP Conf. Ser. Mater. Sci. Eng.* **2020**, *903*, 012042.